Fe-doping and strain effects on structural and magnetotransport properties in $La_{2/3}Ca_{1/3}Mn_{1-y}Fe_yO_3$ thin films

O. Arnache,[1] D. Giratá,[1] and A. Hoffmann[2]
[1]*Institute of Physics, University of Antioquia, A.A. 1226, Medellín, Colombia*
[2]*Materials Science Division, Argonne National Laboratory, Argonne, Illinois 60439, USA*
(Received 5 December 2007; revised manuscript received 23 May 2008; published 23 June 2008)

The influence of ^{57}Fe-doping and strain effects on the structural and magnetotransport properties of undoped and lightly doped ^{57}Fe (1 and 3% at Mn site) $La_{2/3}Ca_{1/3}MnO_3$ thin films and bulk powder samples have been studied. Thin films were grown on (100)-$SrTiO_3$ (STO) and (100)-$LaAlO_3$ (LAO) single crystal substrates, via high O_2 pressure (500 mTorr) using dc magnetron sputtering. Conversion electron Mössbauer (CEM) spectra measured at room temperature in the paramagnetic regime of the Fe-doped samples do not show significant differences in the isomeric shift for the case of the $La_{2/3}Ca_{1/3}MnO_3$ films doped with 1 and 3% iron. The isomeric shift values correspond to the presence of Fe in the 3+ state with octahedral coordination, thus indicating that Fe is incorporated into the structure by substituting Mn. The absence of further states in the spectra indicates that Fe is not involved in forming other additional impurity phases. The x-ray θ-2θ scan showed that all thin films on LAO and STO have single phase and *c*-axis strong orientation along the growth direction and the Fe doping gives rise to a relaxation of the epitaxial strain. Finally, we have observed that the saturation magnetization, Curie temperature, metal-insulator transition, and magnetoresistance vary nonmonotonically with increased Fe concentration. This behavior can be understood in terms of competing influences from the strain relaxation, which enhances the tendency to order ferromagnetically, and the reduced double exchange, which is detrimental to the ferromagnetic order.

DOI: 10.1103/PhysRevB.77.214430 PACS number(s): 75.47.Lx, 74.25.Ha, 76.80.+y, 73.43.Qt

I. INTRODUCTION

The mixed valence perovskite manganites of type $La_{1-x}A_xMnO_3$ (A=divalent ion, such as Ca, Sr, Ba, or Pb) have been extensively investigated because of a wide variety of interesting phenomena such as colossal magnetoresistance (CMR), half-metallicity, and phase separation.[1,2] Perhaps the most prominent phenomena in these compounds is the CMR, which has been first discovered in thin films.[3–5] The CMR manifests itself by a large decrease in the resistivity, when an external magnetic field is applied close to the Curie temperature T_C (Ref. 3). One main focus for theoretical and experimental research on mixed valence manganites is the potential applications, as well as, understanding the physical mechanism responsible for the large magnetoresistance (MR). From an applied point of view it is desirable to increase the values of the MR at low applied magnetic field and to shift the MR peak close to room temperature.[1,2] Among the many explanations of the CMR the model based on Zener's theory of double exchange (DE) is the best established one.[6–8] However, there are experimental and theoretical evidence that suggest that the DE model alone is insufficient to explain the CMR and the other variety of phenomena observed in these compounds.[9]

In this model the unpaired e_g electron in the high spin configuration of Mn^{3+} moves to a neighboring Mn^{4+}. This electron transfer is favored if the Mn^{4+} receives the electron with its spin aligned parallel to the total spin of Mn^{3+}. In this scenario, electron delocalization between Mn ions leads to a lowering of energy and will favor a ferromagnetic ordering of the magnetic moments. For a complete understanding of the magnetic properties it is however important to understand how this double exchange competes with the Mn^{3+}-O-Mn^{4+} superexchange.[7,8] In manganites the doping of a divalent ion, e.g., Ca, onto the La site induces mixed valences of Mn^{3+}/Mn^{4+}, where the Mn^{3+} ions can produce a ferromagnetic double-exchange interaction resulting in the CMR behavior.[1,2] An interesting way to modify the physical properties of these materials is to dope on the Mn site of the crucial Mn^{3+}-O-Mn^{4+} network, which is at the core of double exchange.[10] The introduction of other trivalent (Al, In) or transition metals (Fe, Ni, Co, Cr, Cu, etc.), which introduce a different electronic configuration to the Mn site, shall lead to effects associated with the electronic configuration mismatch between Mn and the other substituting ions. For example, Blasco *et al.*, Sanchez *et al.*, Ghosh *et al.*, and Rivadulla *et al.* have studied the effect of the substitution of Mn with Al, In, Co, and Cr in the magnetoresistive $La_{2/3}Ca_{1/3}MnO_3$ perovskite. They have observed that the compounds became magnetically disordered and inhomogeneous, which was accompanied by structural disorder via the formation of oxygen vacancies in the Mn sublattice as a result of the doping in the Mn site. Besides, they found that the maximum MR is strongly correlated with the lattice parameter and ionic radii of the dopants.[10–13]

Similar to the aforementioned studies, various investigations of electrical, structural, and magnetic properties of polycrystalline, doped manganites have attempted to understand the influence of Fe doping on the magnetotransport behavior. Fe is one of the nearest neighbors of Mn in the periodic table of elements and its ionic radius is close to the Mn ionic radius.[14] In addition, Fe belongs to the third subgroup of elements in the periodic table, and thus both Fe and Mn have similar energy level structure and multiple valence; thus Fe is able to substitute for either Mn^{3+} or Mn^{4+}. Because of this, Fe doping on the Mn site is expected to show inter-

esting physical properties and should provide useful information for understanding the physical mechanisms in these systems. Additionally, Mössbauer spectroscopy (MS) allows microscopic type of measurements, which are particularly relevant and provide information about minute changes in the local electronic, magnetic, and vibrational state of ^{57}Fe via hyperfine interaction. The most relevant past investigations of polycrystalline, Fe-doped manganites are as follows: Leung *et al.* studied a polycrystalline sample of $La_{1-x}Pb_xMn_{1-y}Fe_yO_3$ and observed that magnetic moments of the Fe ions are mostly antiparallel to the Mn magnetization and reduce the magnetization and Curie temperature through the suppression of double exchange.[15] Later, Ahn *et al.* observed a suppression of ferromagnetism and conductivity in both the ferromagnetic (FM) and the antiferromagnetic (AF) phase of $La_{1-x}Ca_xMnO_3$ by doping Fe on the Mn site. Lattice effects, which often dominate doping effects, are negligible in this case due to the nearly identical size of Mn^{3+} and Fe^{3+}. Again the suppression of ferromagnetism and conductivity originates from the reduction of double exchange due to the depopulation of hopping electrons by the Fe doping.[16] Subsequently, Pissas *et al.* and Righi *et al.* studied lightly Fe-doped polycrystalline $La_{1-x}Ca_xMnO_3$ compounds and observed behavior consistent with variable sized FM clusters and AF coupling of the Fe atoms, resulting in a large influence of the Fe doping on the transport properties as well as the magnetic behavior.[17,18] Later, Cai *et al.* found spin-glass behavior with a spin freezing temperature of 42 K close to the metal-insulator transition and CMR effect in the perovskite $La_{0.67}Ca_{0.33}Mn_{0.9}Fe_{0.1}O_3$. These results were ascribed to the formation of FM and AF clusters and the competition between them with the introduction of Fe^{3+} ions, which are not involved in the DE.[19] Afterwards, Ogale *et al.* examined $La_{0.75}Ca_{0.25}Mn_{1-y}Fe_yO_3$ for y values from 0 to 0.05 and suggested that transport in this system involves quasiparticle excitation in association with the DE process and it undergoes localization-delocalization-type transition at a critical dopant concentration.[20] Simopoulos *et al.* have shown that the Fe moments are antiferromagnetically coupled to the ferromagnetic Mn host, when the Fe substitutes for Mn as Fe^{3+} in $La_{2/3}Ca_{1/3}MnO_3$ doped with Fe.[21] Hannoyer *et al.* and Yusuf *et al.* also observed the existence of FM domains in the grain boundary regions of $La_{1-x}Ca_xMn_{1-y}Fe_yO_3$ polycrystalline samples.[22,23]

Remarkably, although the properties of the Fe-doped manganites $La_{1-x}Ca_xMnO_3$ in polycrystalline powder and ceramic samples have been well studied, only very limited studies have been performed on thin films of Fe-doped $La_{2/3}Ca_{1/3}MnO_3$. Huang *et al.* reported an AF arrangement of the Fe and Mn ions over the whole Fe-doping range and a canted spin structure at $y \geq 0.12$ in $La_{0.7}Sr_{0.3}Mn_{1-y}Fe_yO_3$ thin films prepared by pulsed laser deposition. They suggested that increased MR arises from the suppression of enhanced magnetic and polaron scattering under the application of an external field.[24] Finally, Bathe *et al.* have explored the effect of ^{57}Fe ion implantation on the magnetotransport of epitaxial $La_{0.67}Ca_{0.33}MnO_3$ thin films. An increase in the resistance was observed which was attributed to the defects and disorder produced on the surface of the films by Fe ion implantation.[25]

In this study, we investigated Fe doping onto the magnetic Mn lattice site and examined its implications for the structural, magnetic and magnetotransport properties in powders as well as in thin films. Furthermore we studied stress effects due to different thicknesses and substrates. We employed the ^{57}Fe nucleus as a microscopic probe to detect the local behavior of magnetic ions in a series of $La_{2/3}Ca_{1/3}Mn_{1-y}Fe_yO_3$ samples, with $y=0$ (LCMO), 0.01 (LCMFO-1%), and 0.03 (LCMFO-3%). It turns out that the effects of Fe doping and epitaxial stress have competing impacts on structural and magnetotransport properties. The doping relaxes the epitaxial strain efficiently, which is beneficial to FM order, and at the same time inhibits FM order by suppressing double exchange.

II. EXPERIMENTS

The films of $La_{2/3}Ca_{1/3}Mn_{1-y}Fe_yO_3$ ($y=0$, 0.01, and 0.03) used in this study have been grown on $SrTiO_3$ (100) and $LaAlO_3$ (100) single-crystal substrates using *dc* magnetron sputtering. The $La_{2/3}Ca_{1/3}MnO_3$ (LCMO), $La_{2/3}Ca_{1/3}Mn_{0.99}Fe_{0.01}O_3$ (LCMFO-1%), and $La_{2/3}Ca_{1/3}Mn_{0.97}Fe_{0.03}O_3$ (LCMFO-3%) powders for targets were prepared by a standard solid state reaction technique, using high purity (>99.9%) oxide powder of La_2O_3, MnO_2, $CaCO_3$, and Fe_2O_3 96.05% enriched with ^{57}Fe, in order to enhance the Mössbauer signal at the lowest doping level. The powders of these oxides were mixed and heated in air at 1200 °C for several days. All deposition parameters were kept constant for all the films, except the deposition time. During deposition the substrate temperature was kept at 850 °C, the high purity oxygen pressure was 500 mTorr, the substrate-target distance was 40 mm and the deposition power was 40 W. After deposition, the films were cooled down to room temperature in a high-purity oxygen atmosphere at 750 Torr pressure. A series of films LCMO, LCMFO-1% and LCMFO-3% were grown with thicknesses ranging between 23–80 nm.

The structure of the powder for the targets and the deposited films were characterized by high-angle x-ray diffraction (XRD) using a Philips X'PERT PRO diffractometer with Cu $K\alpha$ radiation. The film thicknesses were calculated from grazing incidence x-ray reflectivity measurements. The composition and morphology were analyzed using scanning electron microscopy (SEM) and energy dispersive spectroscopy (EDX).

The local environment of ^{57}Fe atoms in LCMFO-1% and LCMFO-3% target powders and films were investigated by Mössbauer effect (ME) measurements. ME spectra on powder samples were recorded in transmission geometry using a conventional spectrometer with a ^{57}Co(Rh) source of 25 mCi strength moving in a constant acceleration mode at room temperature. The calibration of the spectrometer was made at room temperature using a thin α-Fe foil as the absorber, and the spectra were fitted by using the computer program MOSFT.[26] Conversion electron Mössbauer spectroscopy (CEMS) was used to get information about Fe behavior in the films. CEM spectra were recorded at room temperature using a flowing gas (95% He, 5% CH_4) proportional counter.

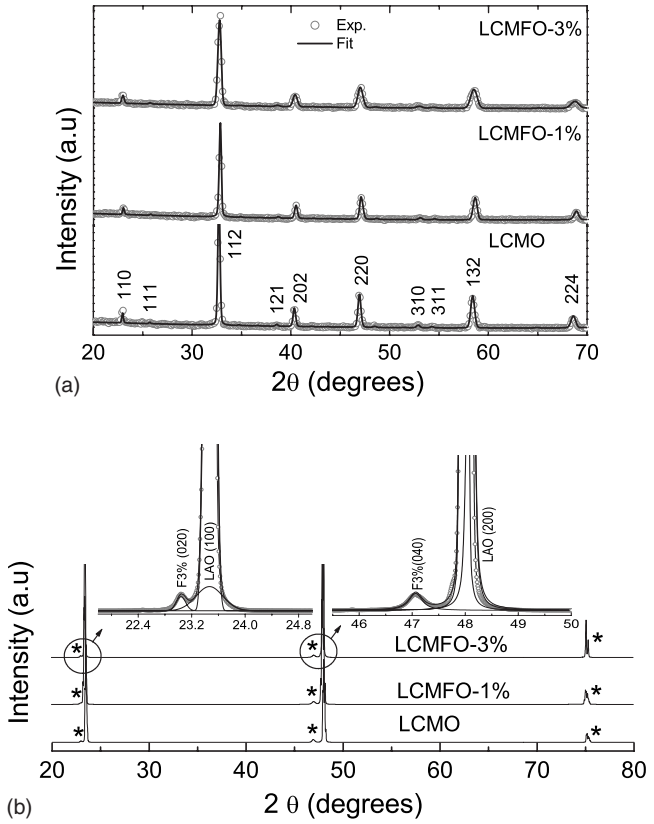

FIG. 1. (a) The XRD spectra of LCMFO-3%, LCMFO-1%, and LCMO powder samples. The open circles are the experimental data, and continuous lines are the fits. For LCMO the Miller indices to the corresponding planes are shown. (b) The XRD spectra of LCMFO-3%, LCMFO-1%, and LCMO thin films grown on $LaAlO_3$ (LAO). Asterisks indicate the manganite peaks and the circles indicate enlarged regions with their respective fits. The fits of experimental data were carried out using Lorentzian and Gaussian functions.

The evaluation of CEM spectra was performed by using MOSSWINN[27] programs.

Transport measurements in the films as a function of temperature ($5 \leq T \leq 300$ K) and magnetic field (from $-5-5$ T) have been carried out in a 6 T transverse superconducting magnet system using a *dc* four-probe method. Electrical contacts were attached to unpatterned films via indium soldering with a 2 mm separation between contacts. Finally, magnetic measurements were carried out with a Quantum Design superconducting quantum interference device (SQUID) magnetometer over a temperature range of 5–300 K. The magnetization vs temperature $M(T)$ in zero field cooling (ZFC) was measured with an applied external magnetic field H of 2 kOe. The $M(H)$ curves were measured from $-1-1$ T at various temperatures in order to investigate the temperature evolution of the coercive fields. In both measurements, the applied magnetic field was parallel to the film surface.

III. RESULTS AND DISCUSSION

The XRD pattern of the LCMO, LCMFO-1%, and LCMFO-3% powders and films are shown in Figs. 1(a) and 1(b) and were collected by scanning over angular range $20 \leq 2\theta \leq 80°$ with steps of 0.01°. The measurements reveal that the three XRD patterns of the $La_{2/3}Ca_{1/3}Mn_{1-y}Fe_yO_3$ powders are single-phase perovskite without detectable secondary phase or impurity, as shown in Fig. 1(a). The refinement of the XRD patterns for the powder samples was carried out by using the MAUD program[28] assuming for all samples the perovskite orthorhombic structure and using the *Pbnm* (62) space group. The fitted lattice parameters are shown in Table I. The *b* and *c* axis of the doped samples are just a little bit smaller than the values for undoped LCMO. Both the lattice parameters and the cell volumes decreased monotonically with Fe doping. These results indicate that the replacement of Mn ions by Fe ions does not have much influence on its lattice because of the identical ion size of Fe^{3+} and Mn^{3+}. A similar behavior was observed by Cai *et al.* for $La_{0.67}Ca_{0.33}Mn_{0.9}Fe_{0.1}O_3$ (Ref. 19). Figure 1(b) shows typical XRD patterns of LCMO, LCMFO-1%, and LCMFO-3% films grown on $LaAlO_3$ (LAO) substrates. XRD patterns on $SrTiO_3$ (STO) are not shown, but are similar. The x-ray θ-2θ scan showed that all thin films on LAO and STO are single phase and are *c*-axis oriented along the growth direction. All reflection peaks corresponding to the thin films on LAO and STO were fitted using Gaussian and Lorentzian functions as shown in the inset of Fig. 1(b). From the fits of the peak positions we calculated the lattice constants of the

TABLE I. Lattice parameters *a*, *b*, and *c* of the LCMO, LCMFO-1%, and LCMFO-3% powder samples.

Targets	*a* (Å)	*b* (Å)	*c* (Å)
LCMO	5.455(8)	5.454(5)	7.707(2)
LCMFO-1%	5.466(1)	5.445(1)	7.686(2)
LCMFO-3%	5.461(2)	5.433(2)	7.670(3)

TABLE II. Thickness *t*, distance between reflection planes *d*, lattice constants *c*, and lattice mismatch δ defined as $[(a_{\text{Subs}} - a_{\text{film}})/a_{\text{Subs}}]^*100\%$, where a_{Subs} are the values for the substrate used, $a_{\text{LAO}}=3.78$ Å, $a_{\text{STO}}=3.9$ Å, and a_{films} are lattice parameters of the perovskite cubic unit cell, which were calculated taking into account that the crystalline structure of LCMO, LCMFO-1%, and LCMFO-3% thin films on LAO and STO, are of orthorhombic type, with lattice parameters $a \sim 2^{1/2}a_{\text{film}}$, $b \sim 2^{1/2}a_{\text{film}}$, and $c=2a_{\text{film}}$.

Films	Thickness (nm)	*d* (Å)	*c* (Å)	δ (%)
LCMO/LAO	23	1.9357(5)	7.743(2)	−2.15(0)
LCMO/LAO	55	1.9336(3)	7.734(5)	−2.03(8)
LCMFO1%/LAO	28	1.9332(6)	7.733(2)	−2.01(2)
LCMFO1%/LAO	60	1.9323(2)	7.729(3)	−1.96(8)
LCMFO3%/LAO	27	1.9311(0)	7.724(1)	−1.90(5)
LCMFO3%/LAO	80	1.9268(3)	7.714(5)	−1.77(8)
LCMO/STO	53	1.9207(2)	7.683(2)	1.62(6)
LCMFO1%/STO	74	1.9280(0)	7.712(1)	1.47(2)
LCMFO3%/STO	70	1.9234(5)	7.695(2)	1.25(5)

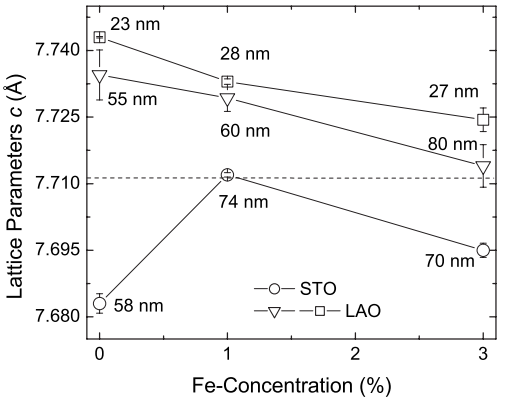

FIG. 2. *c*-axis lattice parameters as a function of Fe concentration in thin films for different thicknesses between 23 and 80 nm on both STO and LAO substrates. The dashed line indicates the lattice constant of undoped LCMO. The triangle and square symbols represent thicker and thinner samples, grown on LAO, respectively, while open circles correspond to samples grown on STO.

unit cell for the films. Table II summarizes the lattice parameters for LCMO, LCMFO-1%, and LCMFO-3% films on STO and LAO. The results from Table II show that with increasing iron concentration, the distance between reflection planes is shifted to lower values, which is qualitatively consistent with the behavior observed for the powder samples. Also, the calculated lattice parameters of the LCMO, LCMFO-1%, and LCMFO-3% thin films grown on the STO and LAO substrates (which have different lattice parameters) reveal the existence of a competition between the epitaxial strain and iron doping effects. Figure 2 shows that the lattice parameters of the films relax with the increasing iron concentration for films grown on both STO and LAO. The strain effects are more notable for the thinnest films. The strain and iron doping effects can be quantified better by calculating the lattice mismatch δ of the films along the interface with regard to the lattice parameters of the substrate (see δ values in Table II). Positive values of δ correspond to tensile strain at the interface, where the unit cell stretches along the plane of the film and is compressed along the growth direction out of the plane. In contrast, negative values describe compressive strain, where the cell stretches along the growth direction and is compressed in the plane of the film.[29] For the case of the films grown on STO, the mismatch decreases, and therefore the lattice parameter relaxes when the iron concentration increases. This indicates that the iron concentration leads to the decrease in the strain-induced distortion of the unit cell. A similar behavior occurs in the films grown on LAO with different thicknesses. Notice that for 1% and 3% Fe doping, the *c*-lattice constant is almost independent of the substrate

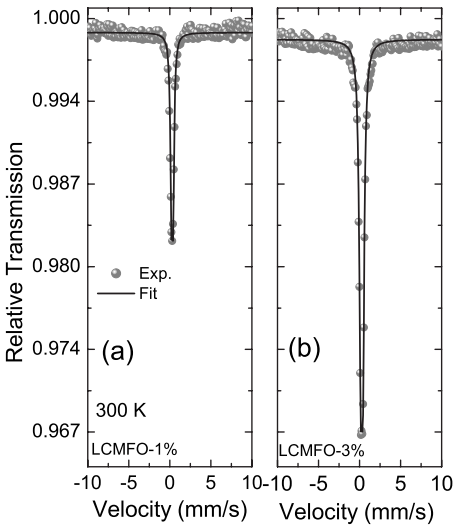

FIG. 3. Transmission Mössbauer spectra of (a) LCMFO-1%, (b) LCMFO-3% powder samples collected at room temperature in the paramagnetic regime. The filled circles are the experimental data and continuous lines are the fits.

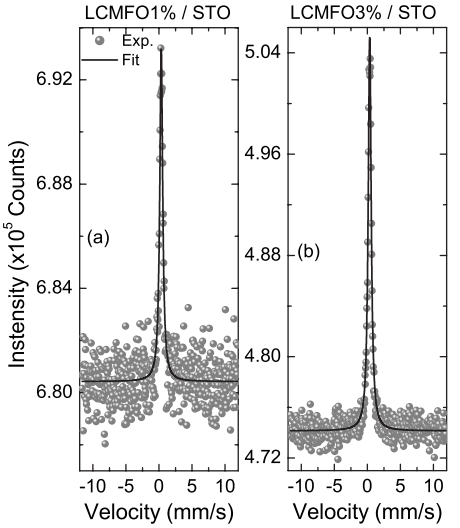

FIG. 4. Typical CEM spectra for (a) LCMFO-1%, (b) LCMFO-3% thin films grown on STO. The filled circles are the experimental data and continuous lines are the fits.

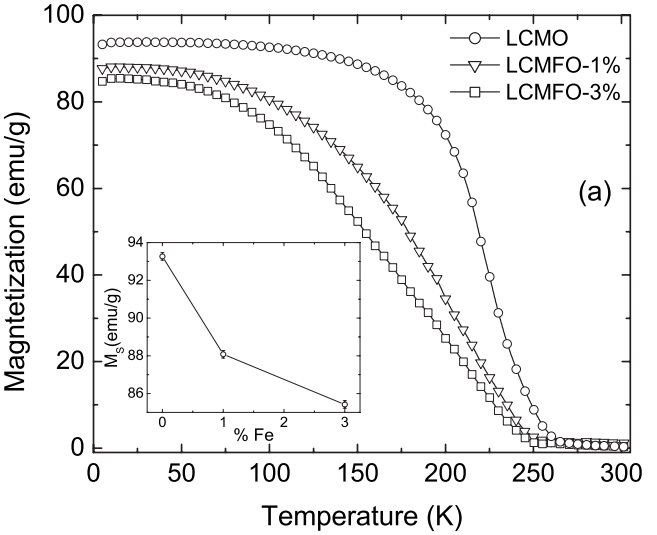

FIG. 5. Temperature dependence of magnetization for LCMO, LCMFO-1%, and LCMFO-3% powder samples at $H=2$ kOe. Inset: the evolution of the saturation magnetization M_S with regard to Fe concentration.

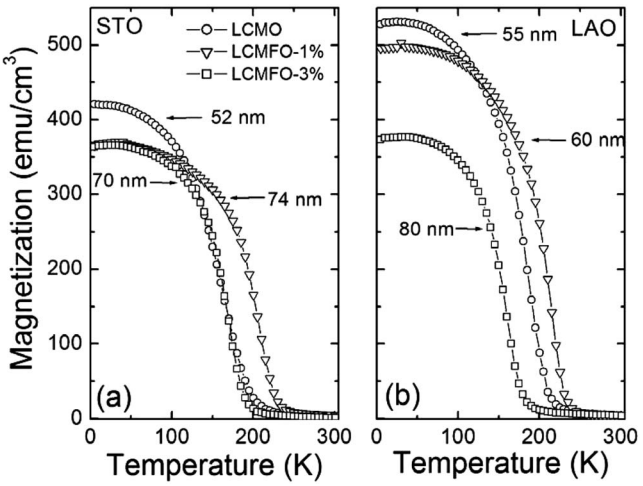

FIG. 6. Magnetization measurements at $H=2$ kOe as a function of temperature for LCMO, LCMFO-1%, and LCMFO-3% thin films. (a) Films grown on STO and (b) films grown on LAO substrate. The thicknesses are (a) LCMO: 52 nm, LCMO-1%: 74 nm, LCMO-3%: 70 nm, and (b) LCMO: 55 nm, LCMO-1%: 60 nm, LCMO-3%: 80 nm.

choice, while there is an appreciable difference for the undoped films. This indicates that while there is significant epitaxial strain for the undoped samples, especially when they are grown on LAO, the epitaxial strain is negligible for the doped films. Therefore the incorporation of Fe gives rise to defects, which effectively relaxes the strain.

Figure 3 shows the Mössbauer spectra of the LCMFO-1% and LCMFO-3% powder samples in the paramagnetic state at room temperature. In both cases the spectra were very similar and consist of a single absorption line typical of paramagnetic behavior. These spectra were fitted with a quadrupole doublet having the following hyperfine parameters: isomer shift $IS=0.32(3)$ mm/s, quadrupolar splitting $QS=0.21(6)$ mm/s, linewidth $w=0.24(1)$ mm/s for LCMFO-1% sample and $IS=0.338(1)$, $QS=0.281(4)$ mm/s, and $w=0.406(6)$ mm/s for LCMFO-3%. The isomer shifts are typical of Fe^{3+} ions in octahedral coordination, while the small quadrupole splitting indicates a slight distortion of the octahedron.[21,30]

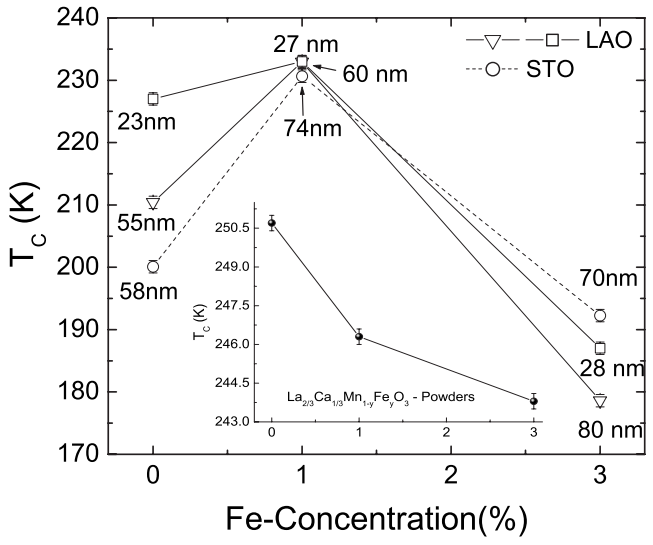

FIG. 7. Fe-doping dependence of T_C for thin films grown on STO and LAO for different thicknesses between 23 and 80 nm. The triangle and square symbols represent the thicker and thinner samples grown on LAO, respectively, while open circles connected with dashed lines correspond to the samples on STO. Inset: Curie temperature as a function of Fe doping of the powder samples.

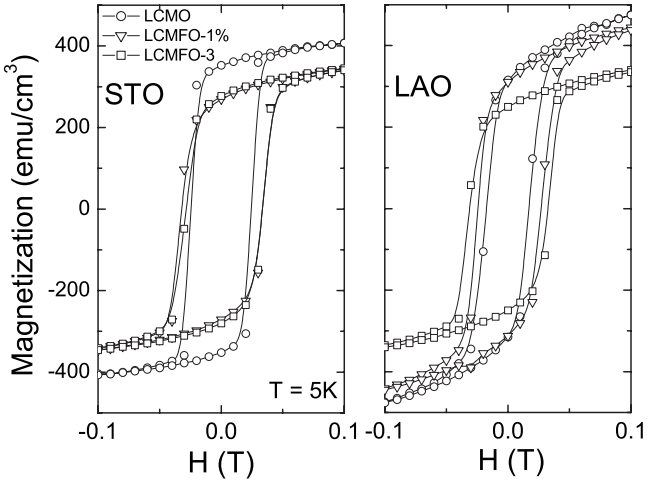

FIG. 8. Magnetic hysteresis loops measured at 5 K for LCMO, LCMFO-1%, and LCMFO-3% thin films. (a) Films grown on STO and (b) films grown on LAO substrate.

In order to analyze the local behavior of iron in the thin film samples, CEM spectra were collected on LCMFO-1% and LCMFO-3% grown on STO. Experimental data of CEM spectra and their respective fits are shown in Fig. 4. The spectrum of LCMFO-1% films was fitted using a singlet with

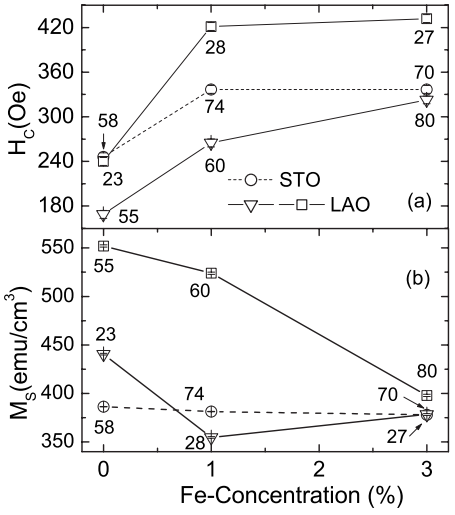

FIG. 9. (a) Coercivity field H_C and (b) the saturation magnetization M_S as a function of Fe concentration for $La_{2/3}Ca_{1/3}Mn_{1-y}Fe_yMnO_3$ thin films doped with different Fe concentration with $y=0$ to 0.03, grown on STO and LAO with different thicknesses. The triangle and square symbols represent the thicker and thinner samples grown on LAO, respectively, while open circles connected with dashed line correspond to the samples on STO.

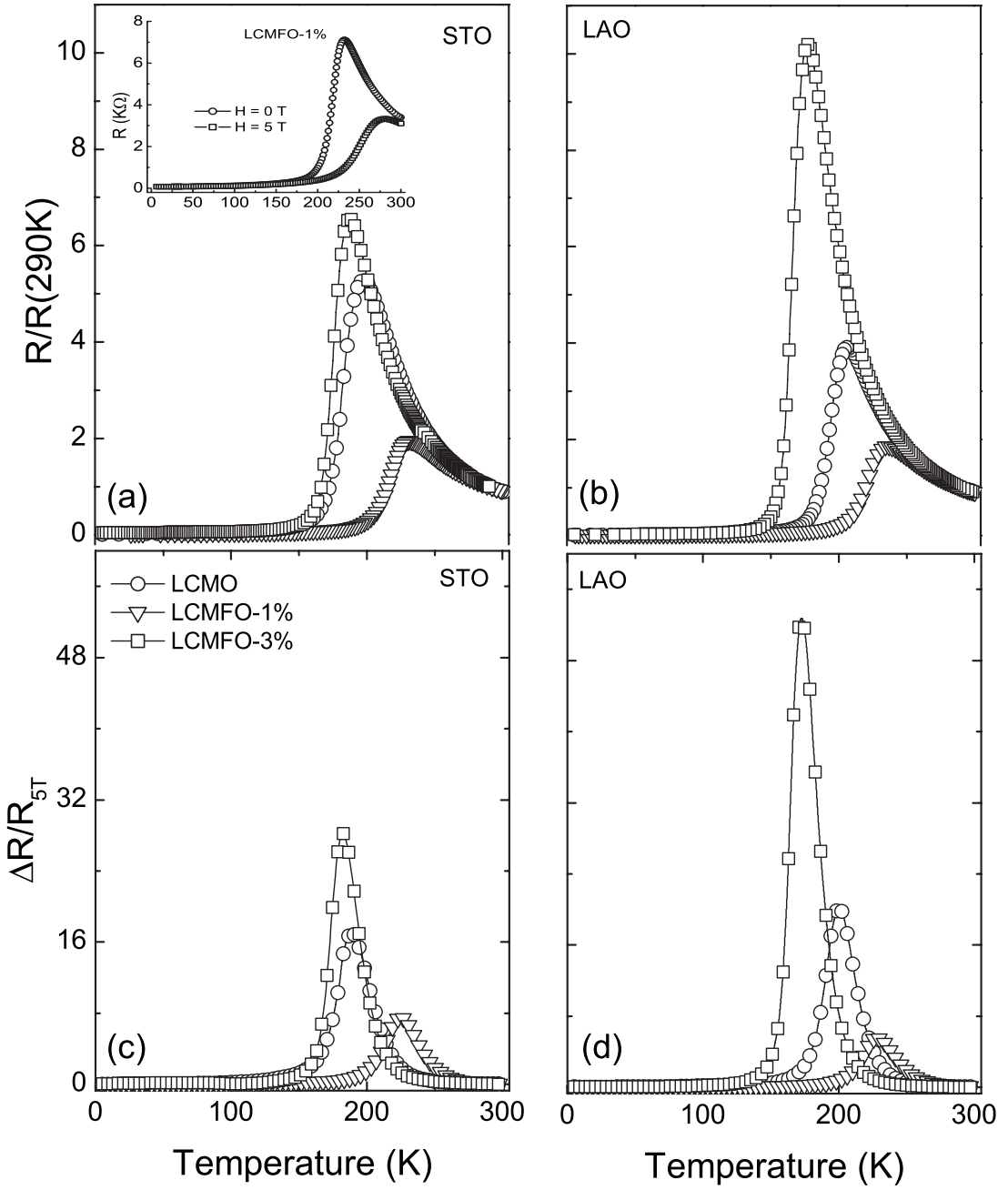

FIG. 10. Temperature dependence of the resistance without external applied magnetic field for LCMO, LCMFO-1%, and LCMFO-3% thin films grown on (a) STO and (b) LAO. To enable a better comparison, all resistance data were normalized to the 290 K values. Magnetoresistance $\Delta R/R_{5T}$ as a function of temperature for LCMO, LCMFO-1%, and LCMFO-3% thin films grown on (c) STO and (d) LAO substrates. Inset: resistance as a function of temperature at $H=0$ T and 5 T magnetic external applied field for LCMFO-1% thin films on STO.

a Lorentzian shape as shown in Fig. 4(a). The relatively noisy baseline is due to the low ^{57}Fe concentration in this weakly doped film. The spectrum shape is typical of a paramagnetic sample, which is the expected behavior at room temperature. From the fits, the hyperfine parameter values are determined to be $IS=0.345(3)$ mm/s and $w=0.525(6)$ mm/s. For the LCMFO-3% films, the CEM spectra are similar to LCMFO-1% films, as Fig. 4(b) shows. In contrast to the samples doped with 1% of Fe, the CEM spectrum for 3% iron doping is better resolved and has less noise for the baseline. Again, the experimental data were fitted using a singlet resulting in hyperfine parameters $IS=0.354(7)$ mm/s and $w=0.537(4)$ mm/s. As for the powder samples the IS values are ~0.35 mm/s, which is consistent with Fe^{3+}, without coexistence of another charge state. However, for the films the site surrounding the iron was found undistorted, in contrast to the observed quadrupolar splitting for the powder samples. This behavior is probably attributed to the epitaxy, which may lead to a better incorporation of the iron ions in the manganite structure.

Furthermore the CEM spectra showed no evidence of other oxide phases which is consistent with the XRD measurements.

The temperature dependencies of the magnetization of the powder samples LCMO, LCMFO-1%, and LCMFO-3% are shown in Fig. 5 and were measured with increasing temperature and an applied field of 2 kOe after cooling from room temperature to 5 K in zero field. The ferromagnetic-paramagnetic phase transition is clearly seen and the transition is very sharp for the undoped sample, while it is broader for the doped samples possibly due to structural disorder in the Mn lattice. A similar behavior was found in samples of $La_{2/3}Ca_{1/3}Mn_{1-x}In_xO_3$ with low In concentration ($x \leq 0.03$) (Ref. 10). The Curie temperature T_C is determined by the inflection point of the magnetization curve vs T. For the undoped sample LCMO we find $T_C \sim 250.7$ K and the saturation magnetization $M_S \sim 93.7$ emu/g. The introduction of Fe doping lowers both T_C and M_S by ~4.5 K and 5.2 emu/g for the 1% Fe-doped sample and ~7.8 K and 7.0 emu/g for the 3% Fe-doped sample (see Fig. 5 and inset). Notice that the relative reduction of the saturation magnetization is slightly larger than what would be expected from the fraction of Mn replaced by Fe. This indicates that not only are the Fe moments oriented antiparallel to the overall ferromagnetically ordered Mn moments, but also the Fe destroys the ferromagnetic order locally.

The temperature dependence of the magnetization of LCMO, LCMFO-1%, and LCMFO-3% thin films is shown in Fig. 6(a) for STO substrates and in Fig. 6(b) for LAO substrates. For all films the T_C values are lower than for the corresponding bulk samples. Remarkably the T_C depends nonmonotonically on the Fe concentration as is also shown in Fig. 7. This behavior of the critical temperature is caused by the competition between the strain relaxation and reduced double exchange due to the Fe doping. Interestingly, the different tensile (STO) and compressive (LAO) strain gives rise to very different T_C values for the undoped films, while for the doped films the T_C is nearly independent of the choice of substrate. This indicates that the Fe doping allows for the strain to be completely relaxed even for the thinnest films.

The hysteresis loops measured at 5 K in LCMO, LCMFO-1%, and LCMFO-3% thin films on STO and LAO are shown in Fig. 8. In both cases, the coercivities increased with Fe doping as is shown in Fig. 9(a), which is consistent with an increased defect density upon doping. These defects may result in increased pinning of domain walls. The Fe-doping dependence of M_S is shown in Fig. 9(b) for LCMO, LCMFO-1%, and LCMFO-3% thin films on STO and LAO. For films with comparable thicknesses the M_S values on LAO are larger than for STO. In contrast to the doping dependence of T_C, M_S still depends on the substrate choice for 1% doping. This probably indicates that for the 1% doping there is still a significant fraction of the film strained close to the interface. But at the 3% doping the epitaxial strain is again completely negligible.

The temperature dependence of the electrical resistance R measured under zero applied magnetic field for the LCMO, LCMFO-1%, and LCMFO-3% thin films grown on STO and LAO are shown in Figs. 10(a) and 10(b). For a better comparison of all curves, they are normalized to the resistance at 290 K. All films show a peak in the resistance, which is associated with a metal-insulator transition.

TABLE III. Metal-insulator transition temperature T_{MI} for $H=0$ and 5 T, thickness and ferromagnetic-paramagnetic transition temperature T_C for LCMO, LCMFO-1%, and LCMFO-3% thin films on STO and LAO.

Films	Thickness (nm)	T_{MI} ($H=0$)	T_{MI} ($H=5$ T)	T_C (K)
LCMO/LAO	23	225.1	277.8	227
LCMO/LAO	55	206.7	256.8	210
LCMFO1%/LAO	27	232.6	284.2	233
LCMFO1%/LAO	60	236.5	279.3	233
LCMFO3%/LAO	28	181.3	244.8	187
LCMFO3%/LAO	80	177.5	234.4	179
LCMO/STO	53	197.8	244.7	200
LCMFO1%/STO	74	232.1	281.0	231
LCMFO3%/STO	70	187.8	240.0	192

Upon applying a 5 T field T_{MI} is significantly decreased for all samples as is shown in Table III. This results in magnetoresistances $MR=\Delta R/R_{5T}=(R_{5T}-R_{0T})/R_{5T}$, which are shown in Figs. 10(c) and 10(d). It is interesting to note that the peak magnitude of MR increases with decreasing T_{MI} and thus the maximum MR shows a nonmonotonic doping dependence mirroring the doping dependence of T_{MI}; see Figs. 11(a) and 11(b). The metal-insulator transition temperature T_{MI} is for all films consistent with T_C obtained from magnetization measurements, i.e., compare Figs. 7 and 11(a) and also see Table III. This means that T_{MI} also shows a nonmonotonic doping dependence reflecting the interplay between strain relaxation and double-exchange suppression. This tendency of MR has also been observed in studies re-

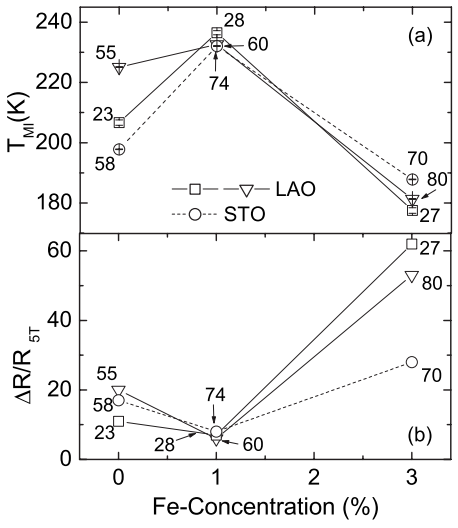

FIG. 11. (a) Fe-doping dependence of metal-insulator transition temperature T_{MI} and (b) MR maximum values, for thin films grown on STO and LAO for different thicknesses between 23 and 80 nm. The triangle and square symbols represent the thicker and thinner samples grown on LAO, respectively, while open circles connected with dashed lines correspond to the samples on STO.

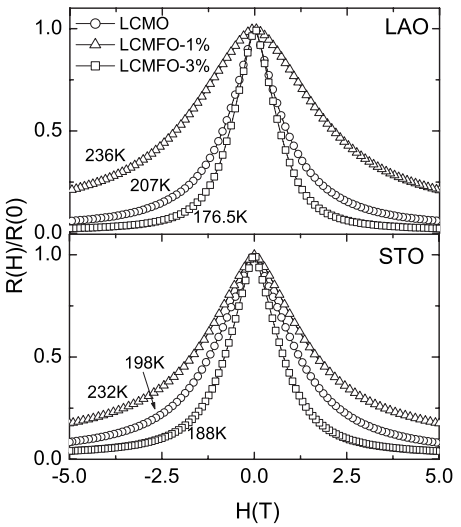

FIG. 12. $R(H)/R(0)$ vs H for LCMO, LCMFO-1%, and LCMFO-3% thin films grown on (a) LAO and (b) STO substrates.

ported on metal transition elements (Cr, Fe, Co, Ni, and Zn) doping effects in $La_{0.7}Ca_{0.3}MnO_3$ polycrystalline manganites.[12] Surprisingly, the maximum *MR* is still very sensitive to the substrate, even for the highest doping, although all the magnetic properties are essentially identical. As can be seen in Figs. 10(c), 10(d), and 11(b) the maximum *MR* for the 3% sample is almost twice as high for samples grown on LAO compared to samples grown on STO. This may indicate that the magnetoresistance could be extremely sensitive to even very small differences in the remaining strain.

Finally, in Fig. 12 we show the relative resistance measurements $R(H)/R(0)$ as a function of external magnetic field measured at the temperatures corresponding to the peaks observed in Fig. 10. We note that the width of the magnetoresistance curves reflect again the nonmonotonic doping dependence and that the width decreases with decreasing T_{MI}.

IV. CONCLUSION

We have grown $La_{2/3}Ca_{1/3}Mn_{1-y}Fe_yO_3$ (y=0, 0.01, and 0.03) thin films on $SrTiO_3$ and $LaAlO_3$ single-crystal substrates using *dc* magnetron sputtering. CEMS measurements showed that Fe is incorporated only in the 3+ state and that there are no significant impurity phases containing Fe. The lattice mismatch between the films and the substrate relaxes in the Fe-doped samples and in turn greatly affects the magnetization and magnetotransport properties. We have observed that the saturation magnetization, Curie temperature, metal-insulator transition, and magnetoresistance vary nonmonotonically with increasing Fe concentration. This behavior can be understood in terms of competing influences from the strain relaxation, which enhance the tendency to order ferromagnetically, and the suppression of double exchange, which is detrimental to the ferromagnetic order.

ACKNOWLEDGMENTS

We would like to acknowledge the assistance of J. E. Pearson and G. Mihailović with the magnetotransport measurements. Furthermore, we acknowledge C. Barrero and K. Nomura for the CEMS measurements. This work was supported by the following: COLCIENCIAS Projects No. 1115-05-17603 and 1115-0517617, CENM Grant No. 043-2005, the Universidad de Antioquia Grant No. SIU-24-1-28 GES in Colombia, and the U.S. Department of Energy, Basic Energy Sciences under Contract No. DE-AC02-06CH11357 at Argonne. O.A. would like to acknowledge the support of COLCIENCIAS and the hospitality he enjoyed at the Argonne National Laboratory.

[1] Yoshinori Tokura, *Colossal Magnetoresistive Oxide* (Gordon and Breach, New York, 2000), Vol. 2.
[2] Elbio Dagotto, *Nanoscale Phase Separation and Colossal Magnetoresistance* (Springer-Verlag, New York, 2002).
[3] R. von Helmolt, J. Wecker, B. Holzapfel, L. Schultz, and K. Samwer, Phys. Rev. Lett. **71**, 2331 (1993).
[4] K. Chahara, T. Onno, M. Kasai, and Y. Kozono, Appl. Phys. Lett. **63**, 1190 (1993).
[5] S. Jin, T. H. Tiefel, M. McCormack, R. Fastnacht, R. Ramesh, and L. H. Chen, Science **264**, 413 (1994).
[6] C. Zener, Phys. Rev. **81**, 440 (1951).
[7] J. B. Goodenouugh, Phys. Rev. **100**, 564 (1955).
[8] P. G. de Gennes, Phys. Rev. **118**, 141 (1960).
[9] A. J. Millis, P. B. Littlewood, and B. I. Shraiman, Phys. Rev. Lett. **74**, 5144 (1995).
[10] J. Blasco, J. Garcia, J. M. de Teresa, M. R. Ibarra, J. Perez, P. A. Algarabel, C. Marquina, and C. Ritter, Phys. Rev. B **55**, 8905 (1997).
[11] M. C. Sanchez, J. Blasco, J. Stankiewicz, J. M. de Teresa, and M. R. Ibarra, J. Solid State Chem. **138**, 226 (1998).
[12] K. Ghosh, S. B. Ogale, R. Ramesh, R. L. Greene, T. Venkatesan, K. M. Gapchup, Ravi Bathe, and S. I., Patil, Phys. Rev. B **59**, 533 (1999).
[13] F. Rivadulla, M. A. Lopez-Quintela, L. E. Hueso, P. Sande, J. Rivas, and R. D. Sánchez, Phys. Rev. B **62**, 5678 (2000).
[14] R. D. Shannon, Acta Crystallogr., Sect. A: Cryst. Phys., Diffr., Theor. Gen. Crystallogr. **32**, 751 (1976).
[15] L. K. Leung, A. H. Morrish, and B. J. Evans, Phys. Rev. B **13**, 4069 (1976).
[16] K. H. Ahn, X. W. Wu, K. Liu, and C. L. Chien, Phys. Rev. B **54**, 15299 (1996).
[17] M. Pissas, G. Kallias, E. Devlin, A. Simopoulos, and D. Niarchos, J. Appl. Phys. **81**, 5770 (1997).
[18] L. Righi, P. Gorria, M. Insausti, J. Gutierrez, and J. Barandiarán, J. Appl. Phys. **81**, 5767 (1997).
[19] Jian-Wang Cai, Cong Wang, Bao-Gen Shen, Jian-Gao Zhao, and Wen-Shan Zhan, Appl. Phys. Lett. **71**, 1727 (1997).
[20] S. B. Ogale, R. Shreekala, Ravi Bathe, S. K. Date, S. I. Patil, B. Hannoyer, F. Petit, and G. Marest. Phys. Rev. B **57**, 7841 (1998).

[21] A. Simopoulos, M. Pissas, G. Kallias, E. Devlin, N. Moutis, I. Panagiotopoulos, D. Niarchos, C. Christides, and R. Sonntag, Phys. Rev. B **59**, 1263 (1999).
[22] B. Hannoyer, G. Marest, J. M. Greneche, Ravi Bathe, S. I. Patil, and S. B. Ogale, Phys. Rev. B **61**, 9613 (2000).
[23] S. M. Yusuf, M. Sahana, M. S. Hegde, K. Dörr, and K. H. Müller, Phys. Rev. B **62**, 1118 (2000).
[24] Q. Huang, Z. W. Li, J. Li, and C. K. Ong, J. Phys.: Condens. Matter **13**, 4033 (2001).
[25] Ravi Bathe, S. I. Patil, K. P. Adhi, B. Hannoyer, and G. Marest, J. Appl. Phys. **93**, 1127 (2003).
[26] W. A. Dollase, Am. Mineral. **60**, 257 (1975).
[27] Z. Klencsár, E. Kuzmann, and A. Vértes, J. Radioanal. Nucl. Chem. **210**, 105 (1996).
[28] MAUD, Materials Analysis Using Diffraction, by L. Lutterotti, Version 1.84, 2002 (http://www.ing.unitn.it/~maud/).
[29] Milton Ohring, *Materials Science of Thin Films, Deposition and Structure*, 2nd ed. (Academic, San Diego, CA, 2002), p. 423.
[30] R. E. Vandenberghe, *Mössbauer Spectroscopy and Applications in Geology* (State University Gent, Belgium, 1990), Vol. 8.